



1 **The Microfluidic Ice Nuclei Counter Zürich (MINCZ): A** 2 **platform for homogeneous and heterogeneous ice nucleation**

3 Florin N. Isenrich^{1*}, Nadia Shardt^{2*}, Michael Rösch², Julia Nette¹, Stavros Stavrakis¹, Claudia
4 Marcolli², Zamin A. Kanji², Andrew J. deMello¹, Ulrike Lohmann²

5 ¹Institute for Chemical and Bioengineering, ETH Zurich, Zürich, 8093, Switzerland

6 ²Institute for Atmospheric and Climate Science, ETH Zurich, Zürich, 8092, Switzerland

7
8 *These authors contributed equally to this work.

9 **Correspondence:** Nadia Shardt (nadia.shardt@env.ethz.ch) and Andrew J. deMello
10 (andrew.demello@chem.ethz.ch)

11
12
13 **Abstract.** Ice nucleation in the atmosphere is the precursor to important processes that determine cloud properties
14 and lifetime. Computational models that are used to predict weather and project future climate changes require
15 parameterizations of both homogeneous nucleation (i.e., in pure water) and heterogeneous nucleation (i.e.,
16 catalysed by ice-nucleating particles, INPs). Microfluidic systems have gained momentum as a tool for obtaining
17 such parameterizations and gaining insight into the stochastic and deterministic contributions to ice nucleation. In
18 this regard, polydimethylsiloxane (PDMS) devices are typically used to generate droplets in microchannels that
19 are then cooled and monitored “on-chip”. However, using PDMS has two drawbacks. First, it has a low thermal
20 conductivity that generates temperature gradients within a PDMS chip upon cooling from below, which can lead
21 to increased temperature uncertainty at the droplets’ location. Second, it readily absorbs water and is gas
22 permeable, which compromises the stability of droplets over extended timescales. To overcome these
23 shortcomings, we have developed a new instrument: the Microfluidic Ice Nuclei Counter Zürich (MINCZ). In
24 MINCZ, droplets are generated using a PDMS chip, but are then stored in fluoropolymer tubing that is relatively
25 impermeable to water and solvents. Droplets within the tubing are cooled in an ethanol bath that ensures efficient
26 heat transfer and reduces uncertainty in droplet temperature. Herein, we describe the design of MINCZ, which
27 fulfils the following requirements: (i) high accuracy and precision in measuring droplet temperatures within 0.2 K;
28 (ii) ability to reach the homogeneous freezing point of pure water, with a median freezing temperature of
29 237.3 ± 0.1 K for droplets with a diameter of 75 μm ; and (iii) the ability to simultaneously perform several freeze–
30 thaw cycles on hundreds of droplets. These characteristics allow to narrow the reported spread in nucleation rates
31 as a function of temperature in past work, to detect mediocre and poor ice-nucleating particles at any temperature
32 above that of homogeneous freezing, and to investigate the stochastic behaviour of nucleation. We validate
33 MINCZ by measuring homogeneous freezing temperatures of water droplets and heterogeneous freezing
34 temperatures of aqueous suspensions containing microcline, a common and effective INP in the atmosphere. In
35 the future, MINCZ will be used to investigate the stochastic and deterministic behaviour of INPs, motivated by a
36 need for better-constrained parameterizations of ice nucleation in weather and climate models, where the presence
37 or absence of ice influences cloud optical properties and precipitation formation.

38



39 **1 Introduction**

40 Water in mixed-phase clouds is present in both the liquid and crystalline form, and the proportion between cloud
41 droplets and ice crystals alters cloud radiative properties as well as cloud lifetimes (Lohmann, 2017; Lohmann
42 and Feichter, 2005; Matus and L'Ecuyer, 2017). The transformation of liquid to ice in the troposphere can occur
43 via homogeneous nucleation (in a pure water or aqueous droplet) or heterogeneous nucleation (for example, in a
44 droplet containing solid particles). While homogeneous freezing of supercooled water occurs at temperatures
45 below about 238 K, depending on droplet size and relative humidity (Ickes et al., 2015; Koop et al., 2000;
46 Kreidenweis et al., 2018), heterogeneous nucleation in mixed-phase clouds may occur at temperatures up to 273 K
47 in aqueous droplets containing impurities (ice-nucleating particles, INPs) that catalyse ice formation. Conversely,
48 the presence of salt ions in solution may lead to a freezing point depression below the corresponding pure-water
49 homogeneous or heterogeneous freezing temperature (Koop et al., 2000; Zobrist et al., 2008). A number of INP
50 types are known to originate from natural and anthropogenic sources, including minerals such as feldspars, clay
51 minerals, organic macromolecules, and organic matter (Kanji et al., 2017). However, the exact roles of the
52 stochastic (time-dependent) and deterministic (time-independent) contributions to heterogeneous ice nucleation
53 are uncertain and necessitate further research (Kaufmann et al., 2017; Knopf et al., 2020; Wright and Petters,
54 2013). A better understanding of these processes could improve our understanding of the role of INPs in
55 precipitation formation so that present uncertainties in climate projections and weather forecasts may be reduced.
56 In fact, the role of INPs in aerosol–cloud interactions has recently been identified as a research priority in the
57 atmospheric community (Murray et al., 2021). Beyond the atmosphere, a more complete knowledge of ice
58 nucleation is also pertinent to applications such as cryopreservation (Marquez-Curtis et al., 2021; Pegg, 2015) and
59 pharmaceutical manufacturing (Assegehegn et al., 2019; Deck et al., 2022).

60
61 A range of techniques has been developed to study homogeneous and heterogeneous nucleation in atmospherically
62 relevant systems (Diehl et al., 2014; Kaufmann et al., 2016; Miller et al., 2021; Rogers, 1988; Stetzer et al., 2008),
63 and each technique can be associated with a particular drawback. For example, single-particle levitation devices
64 (Diehl et al., 2014; Krämer et al., 1996) are time-consuming for investigating a large number of droplets sufficient
65 for statistical analysis, whereas differential scanning calorimetry measurements of water-in-oil emulsions
66 typically give only qualitative insight into nucleation behaviour due to the polydispersity in droplet size
67 (Kaufmann et al., 2016; Klumpp et al., 2022; Kumar et al., 2018). To overcome such shortcomings, microfluidic
68 techniques can be used to generate a stable, monodisperse population of water droplets at high throughput, suitable
69 for quantifying nucleation rates. Water-in-oil emulsions are generated at an orifice, where the oil phase cleaves
70 off the water phase to generate a droplet. Nonionic surfactants dispersed in the oil phase stabilize the droplets at
71 the oil–water interface. At the microfluidic size scale, it becomes possible to investigate homogeneous ice
72 nucleation, low INP concentrations, and INPs with mediocre or poor activity. Moreover, since microfluidic
73 systems allow for the high-throughput generation of water-in-oil droplets, the number of droplets studied with this
74 technique outnumbers the standard 96-well plates employed in many traditional droplet-freezing assays (e.g.,
75 David et al. (2019), Schneider et al. (2021), Garcia et al. (2012), and Kunert et al. (2018); see Miller et al. (2021)
76 for a full list). Briefly, we note that the term cloud droplet denotes diameters up to approximately 50 μm in
77 atmospheric science, while in microfluidics, a droplet can refer to larger sizes up to the nL range; hereafter, we
78 refer to droplets more generally, not restricted to cloud droplet sizes.



79

80 Amongst existing microfluidic platforms designed for studying ice nucleation, there are two common approaches
81 for droplet generation and cooling: dynamic flow-through devices (Roy et al., 2021a; Stan et al., 2009; Tarn et al.,
82 2020, 2021) and static droplet arrays (Brubaker et al., 2019; Edd et al., 2009; Reicher et al., 2018; Roy et al.,
83 2021b). The flow-through approach is beneficial for analysing high numbers of droplets (between 10^3 and 10^4
84 (Tarn et al., 2020)) and therefore is particularly suitable for detecting low concentrations of INPs suspended in
85 water or an aqueous solution. Continuous flow devices are also desirable for potential use as autonomous in-line
86 instruments for monitoring the temporal evolution of INP concentration in the field (Tarn et al., 2020). One
87 drawback of current flow-through devices is the difficulty in independently controlling the cooling rate of droplets
88 over orders of magnitude. This is due to the fact that cooling rates are a function of fluid flow rate and channel
89 length, and changing these variables will also affect droplet diameter. A second drawback associated with
90 continuous flow devices is the inability to perform refreeze experiments on the produced droplets. On the other
91 hand, static droplet arrays are not suitable for detecting rare INPs in solution since such arrays generally only
92 contain between 10^2 and 10^3 droplets per experiment, and it is statistically unlikely for a rare INP to be present in
93 such a small volume of liquid (Brubaker et al., 2019; Reicher et al., 2018). Droplet arrays are beneficial in that
94 they can be cooled at various rates in a controllable fashion, providing the option of multiple cooling and thawing
95 cycles to gain insight into the stochastic vs. deterministic behaviour of heterogeneous ice nucleation.

96

97 In both flow-through and droplet array designs, microfluidic devices are almost always fabricated from
98 polydimethylsiloxane (PDMS) and plasma bonded to glass slides. PDMS is a hydrophobic, non-porous and gas-
99 permeable material. This gas permeability, however, can lead to the rapid evaporation and concomitant shrinking
100 of water droplets, limiting refreezing experiments.. Droplet evaporation can be reduced with various surface
101 treatments (Brubaker et al., 2019) or a blocking layer of a different material (Heyries et al., 2011), but to
102 permanently prevent gas permeation, alternative substrate materials must be considered. One alternative strategy
103 is to cool droplets off-chip on a solid substrate while covering them with a fluid of low gas-permeability like
104 silicone oil or squalene (Peckhaus et al., 2016; Wright and Petters, 2013). A second alternative is to store droplets
105 off-chip in tubing and immerse the tubing in an ethanol bath for cooling, as shown by Atig et al. (2018). It should
106 be noted that, in this study, droplet diameters were more than 1 mm, with the median freezing point of water at
107 this size being 249 K (-24 °C), i.e., far above homogeneous ice nucleation temperatures.

108

109 In cold-stage microfluidic platforms, droplets are typically cooled from below. Such an approach takes advantage
110 of the excellent heat transfer that accompanies miniaturisation, yet it is hampered by the poor heat transfer through
111 PDMS, which gives rise to a temperature gradient within the microfluidic device (Polen et al., 2018). Therefore,
112 measuring the actual temperature of droplets within the device remains a challenge, since cooling a microfluidic
113 device directly from the bottom generates a temperature gradient within the device. To account for such
114 temperature differentials, Reicher et al. (2018) calibrated droplet temperatures as a function of cold-stage
115 temperature by observing the melting of solutions and materials with known melting points. As discussed by
116 Reicher et al. (2018), a different calibration equation was needed for each PDMS substrate thickness, which was
117 identified by Polen et al. (2018) as a potential drawback. To avoid a thickness-dependent calibration, Tarn et al.
118 (2020, 2021) placed a thermocouple within a microfluidic channel parallel to the one through which droplets flow



119 to more accurately determine droplet temperature, but the reported uncertainty in this setup is still at a relatively
120 high value of ± 0.7 K. Given that uncertainties in homogeneous ice nucleation rates are dominated by uncertainties
121 in temperature (Riechers et al., 2013), increasing an instrument's temperature accuracy is the single most
122 important factor in improving our ability to precisely discern how nucleation rate changes as a function of
123 temperature. This is especially important because nucleation rates for the homogeneous freezing of water obtained
124 from various instrument types (continuous flow chambers, droplet freezing assays, etc.) and instruments of the
125 same type (e.g., all microfluidic platforms) currently span several orders of magnitude at the same temperature
126 (Ickes et al., 2015; Tarn et al., 2021).

127

128 Amongst the rapidly-growing number of microfluidic systems designed to investigate ice nucleation, we aimed
129 to develop a setup able to create and freeze picoliter-sized droplets, whilst avoiding the primary disadvantages
130 associated with current methods. Namely, our goals were to achieve a monodisperse size distribution of droplets
131 with diameters of $75 \mu\text{m}$, generate a large number of droplets (many hundreds), ensure droplet stability over the
132 time needed to perform multiple (re-)freezing cycles at various cooling rates, minimize temperature gradients in
133 the device, and ensure high accuracy and precision in all temperature measurements. Further, and most
134 importantly, we aimed to develop a system that is easy to handle and easy to transfer to other laboratories or field
135 sites. Herein, we present and validate our system and technique. We report data for the homogeneous freezing of
136 pure water and for the heterogeneous freezing of microcline suspensions in water. Microcline, a K-feldspar, is
137 selected as an example, since it is commonly found in collected mineral dust samples and it is a highly active INP
138 (Harrison et al., 2016; Kanji et al., 2017; Klumpp et al., 2022; Welte et al., 2019).

139 **2 Materials and Methods**

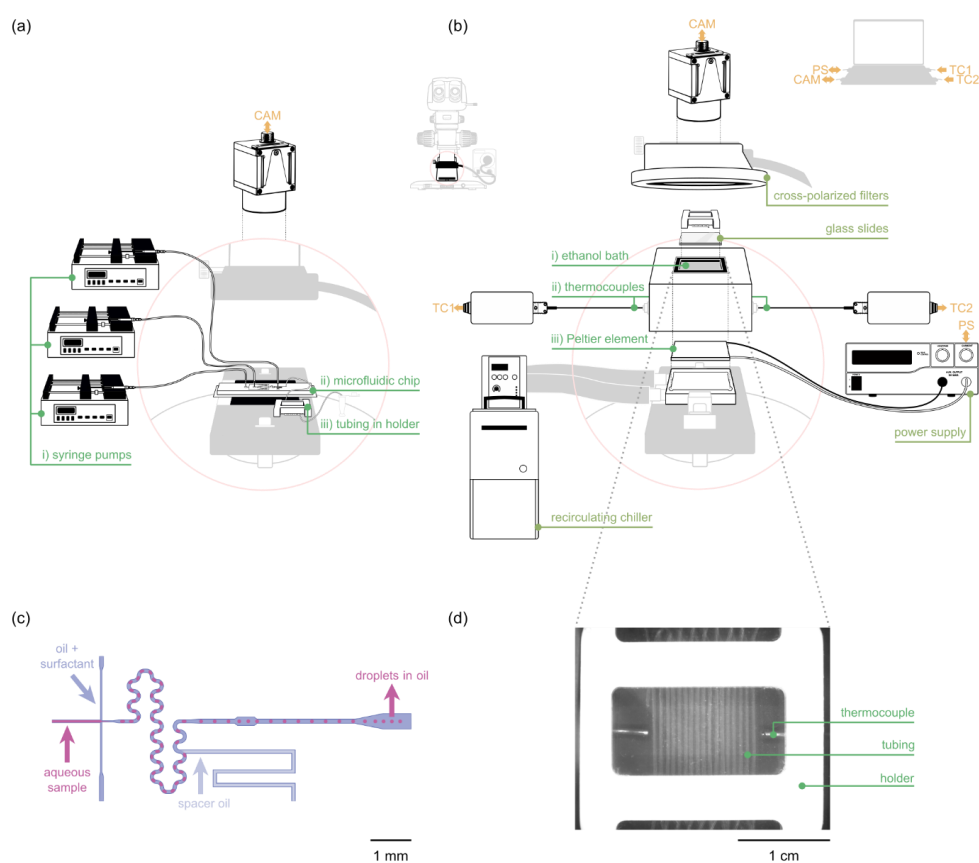
140 In the Microfluidic Ice Nuclei Counter Zürich (MINCZ), droplets are generated in a conventional PDMS
141 microfluidic device. Droplets are not stored on-chip, but in fluorinated (perfluoroalkoxy alkane, PFA) tubing
142 having an inner diameter of $75 \mu\text{m}$. The PFA tubing is immersed and cooled in an ethanol bath, minimizing any
143 temperature gradients, while maximizing heat transfer. The chemically inert and relatively gas-impermeable PFA
144 tubing allows for prolonged cooling cycles and refreeze experiments to temperatures below which pure water
145 freezes homogeneously. A CMOS camera connected to a stereoscope is used to image the droplets and a semi-
146 automated image analysis algorithm is used to identify droplet freezing events. We present a general summary of
147 the components that comprise MINCZ (Sect. 2.1), followed by detailed descriptions of the microfluidic chip
148 (Sect. 2.2) and aqueous sample preparation (Sect. 2.3). Finally, the workflow of a typical experiment is presented,
149 including droplet generation (Sect. 2.4.1), droplet cooling (Sect. 2.4.2), and image analysis to determine droplet
150 size (Sect. 2.4.3) and freezing temperature (Sect. 2.4.4).

151 **2.1 Instrument design**

152 Figure 1 presents an overview of the equipment used in MINCZ. Each piece of equipment is categorized based
153 on its function, whether it is used during droplet generation (Fig. 1a and 1c) or droplet cooling (Fig. 1b and 1d).
154 A stereoscope (Nikon SMZ1270, $0.5\times$ objective lens, fibre ring illuminator with LED light source) connected to
155 a CMOS camera (iDS UI-3060CP-M-GL Rev. 2) is used in both steps to obtain images. For droplet generation



156 (see Sect. 2.4.1 for more details), we use: i) three syringe pumps fitted with 1 mL glass syringes; ii) a PDMS
157 microfluidic chip; and iii) high-purity perfluoroalkoxy alkane (PFA) tubing that is directly inserted into the outlet
158 of the microfluidic chip and kept in place in a custom-milled polyether ether ketone (PEEK) holder. For droplet
159 cooling (see Sect. 2.4.2 for more details), we use: i) an ethanol cooling bath (insulated by a custom 3D-printed
160 structure) to immerse the droplet-containing PFA tubing; ii) two K-type thermocouples; iii) a Peltier element
161 connected to a power supply and cooled from below by a heat transfer fluid circulating through an aluminium
162 block connected to a chiller. To improve image quality during droplet cooling, we use a pair of cross-polarized
163 filters, and we place six glass cover slips underneath the PEEK tubing holder for improved image contrast.



164
165 **Figure 1. Overview of the Microfluidic Ice Nuclei Counter Zürich (MINCZ) equipment grouped into (a) the droplet**
166 **generation step with (i) syringe pumps, (ii) a microfluidic chip, and (iii) PFA tubing in a PEEK holder; and (b) the**
167 **droplet cooling zone with (i) an ethanol bath, (ii) two thermocouples, and (iii) a Peltier element. (c) A schematic of the**
168 **microfluidic channels used to generate aqueous droplets surrounded by an oil–surfactant continuous phase. (d) A**
169 **top-down image of the ethanol bath into which the PEEK holder with PFA tubing is placed.**

170 2.2 Microfluidic chip design and fabrication

171 The microfluidic chip design was drawn in AutoCAD® 2018 (Autodesk, San Rafael, USA). It features a flow-
172 focusing droplet generator with an orifice that is 75 μm high and 20 μm wide. After passing through passive-



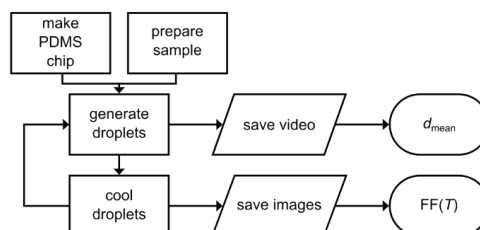
173 mixing structures, the droplets flow from a 350 μm wide outlet into the 75 μm inner diameter PFA outlet tubing.
174 A schematic representation is shown in Figure 1c. The chip design was printed onto a high-resolution film
175 photomask (Micro Lithography Services Ltd, Chelmsford, UK) which was used to pattern an SU-8 (GM1070,
176 Gersteltec, Switzerland) coated silicon wafer (10 mm diameter, 525 ± 25 thickness, <100> orientation, Siegert
177 Wafer GmbH, Germany). This resulting master mould was employed to fabricate the PDMS chips by pouring
178 PDMS (Elastosil RT 601 A/B, Ameba AG, Switzerland) over the mould at a 10:1 mass ratio of base to curing
179 agent, with subsequent curing at 70 °C for more than two hours. Inlets (0.76 mm) and outlets (0.41 mm) were
180 punched with a hole-puncher (Shafts 20 and 25, Syneo, USA), and the PDMS devices were plasma bonded
181 (plasma cleaner, Diener electronic GmbH, Germany) to planar glass slides (Menzler-Glaser, Germany). To
182 improve hydrophobicity, the PDMS devices were incubated in 5 % v/v (tridecafluoro-1,1,2,2-
183 tetrahydrooctyl)trichlorosilane (97 %, aber GmbH, Germany) for 5 minutes, then in HFE-7500 (3M™ Germany)
184 for 5 minutes, and then kept on a hot plate at 120 °C for at least 14 hours.

185 2.3 Sample preparation

186 For the homogeneous freezing assays, ultrapure water was used (molecular biology reagent-grade, 0.1 μm filtered,
187 Sigma–Aldrich, USA), hereafter referred to as Sigma–Aldrich (SA) water. The microcline used in the
188 heterogeneous ice nucleation experiments was from the same milled stone from Elba, Italy, as reported in a
189 previous study (Welti et al. (2019); for mineralogical composition, see X-ray diffraction results therein). Scanning
190 electron microscopy (SEM) revealed a high size-polydispersity of the mineral particles ranging from sub-
191 micrometer to more than 30 μm (Fig. A1a). Indeed, individual particles were clearly visible when suspended in
192 microfluidic droplets (Fig. A2). To ensure repeatability and reproducibility, we homogenized the microcline to
193 particles in the sub-micrometer range using the following procedure. First, the mineral sample (2 g in 50 mL SA
194 water) was sonicated (8×30 s pulse in a UP200ST ultrasonic VialTweeter (Hielscher Ultrasonics GmbH,
195 Germany)) followed by filtration using a 0.45 μm polyethersulfone sterile syringe filter (TPP Techno Plastic
196 Products AG, Switzerland). Then, the resulting homogeneous mineral sample was concentrated and dried using a
197 SpeedVac (Savant™ SPD111V, Thermo Scientific™, USA). Just before use, the resulting pellet of mineral
198 particles was rehydrated to a stock solution of 1.5 mg mL^{-1} in SA water, and this stock solution was subsequently
199 diluted to the working solution of 0.5 mg mL^{-1} and sonicated in a water bath for 15 minutes. The size distribution
200 of the microcline particles was visualized using scanning electron microscopy (SEM; FEI Magellan 400 Scanning
201 Electron Microscope), as shown in Fig. A1c.

202 2.4 Experimental workflow

203 Figure 2 summarizes the workflow of an experiment using MINCZ. Spherical water-in-oil droplets are generated
204 within a PDMS chip (see Sect. 2.4.1 for details) and introduced into the PFA tubing. A video is recorded during
205 droplet generation, from which the mean droplet diameter can be evaluated (see Sect. 2.4.3). Afterwards, the
206 droplet population within the PFA tubing is cooled in the ethanol bath, while images are captured at a frequency
207 sufficient to obtain one image for every 0.05 K decrease in temperature, depending on the user-specified cooling
208 rate (see Sect. 2.4.2). We process the saved images using a semi-automated image analysis algorithm to determine
209 the number of frozen droplets as a function of temperature (see Sect. 2.4.4).



210
211 **Figure 2.** Workflow of an experiment using MINCZ consisting of PDMS chip fabrication and sample preparation,
212 followed by droplet generation and cooling, where a high-speed video is taken to determine mean droplet diameter
213 and a series of images are taken to determine the frozen fraction (FF) of droplets as a function of temperature.

214 2.4.1 Droplet generation

215 As seen in Figure 1a and 1c, the PDMS microfluidic chip is connected to two pieces of PTFE tubing (0.56 mm
216 ID, 0.25 mm OD, Rotima AG Switzerland) containing the water phase and the surfactant in oil (5 % 008-
217 FluoroSurfactant (RAN Biotechnologies, USA) diluted to 1 % v/v in HFE-7500) for droplet generation, while a
218 third piece of tubing containing fluorinated oil (HFE-7500) is employed as a spacer fluid. Glass syringes (1 mL
219 Hamilton® syringe, Sigma–Aldrich, USA) are filled with a supporting fluid (either water or fluorinated oil) and
220 held in syringe pumps (Aladdin AL1000-220Z, World Precision Instruments, USA), which are employed to ensure
221 stable flow rates. An air bubble between each injected fluid (the aqueous sample and the surfactant–oil mixture)
222 and the supporting fluid in the PTFE tubing prevents contamination and dilution of the sample by the supporting
223 fluid, whilst allowing for flexible and low sample consumption. One end of the PFA tubing for droplet storage
224 (50 cm in length, 360 µm OD, 75 µm ID, IDEX Health & Science LLC, USA) is directly inserted into the PDMS
225 device outlet. The rest of the tubing is kept in the custom-milled PEEK holder. During droplet generation, the
226 PDMS device is monitored using the stereoscope and camera. After a stable generation of spherical droplets is
227 achieved and a video of droplet generation is recorded, the PFA tubing is immediately cut from the PDMS chip
228 with scissors, and the tubing ends mechanically blocked using tweezers.

229

230 The flowrates used in the current study are listed in Table 1 for the SA water experiments and Table 2 for the
231 microcline experiments. The same PDMS chip can be reused for several consecutive runs (e.g., for the generation
232 of the three microcline suspensions in Table 2), or separate chips may be used if channels become clogged between
233 experiments or if the chip delaminates from the glass slide due to insufficient bonding (e.g., in Table 1). As a
234 result of new chips being used from one day to another, the flow rates in Table 1 and Table 2 required for stable
235 droplet generation differ slightly.

236



237 **Table 1: Sigma–Aldrich (SA) water, surfactant in oil, and spacer oil flowrates used to produce each population of**
238 **droplets for the homogeneous freezing experiments. The mean diameter of droplets obtained from the captured high-**
239 **speed video is also summarized for each droplet population.**

	Q_{water} [$\mu\text{L min}^{-1}$]	$Q_{\text{surfactant}}$ [$\mu\text{L min}^{-1}$]	$Q_{\text{spacer oil}}$ [$\mu\text{L min}^{-1}$]	d_{mean} [μm]
day 1	1.0	1.5	2.0	75 ± 5
day 2	1.0	1.5	2.3	75 ± 5
day 3	1.0	2.0	1.4	78 ± 5

240

241 **Table 2: Microcline suspension, surfactant in oil, and spacer oil flowrates used to produce each population of droplets**
242 **for the heterogeneous freezing experiments. The mean diameter of droplets obtained from the captured high-speed**
243 **video is also summarized for each droplet population.**

	$Q_{\text{microcline}}$ [$\mu\text{L min}^{-1}$]	$Q_{\text{surfactant}}$ [$\mu\text{L min}^{-1}$]	$Q_{\text{spacer oil}}$ [$\mu\text{L min}^{-1}$]	d_{mean} [μm]
i	0.8	1.5	2.3	78 ± 5
ii	0.8	1.5	2.3	73 ± 5
iii	0.9	1.5	2.3	73 ± 5

244 2.4.2 Droplet cooling

245 The PFA tubing containing the droplets is immersed in an ethanol bath held in an aluminium container (40 mm ×
246 40 mm × 60 mm). The inside walls of the bath are oxidized to provide a black background behind the droplets to
247 improve imaging contrast. Six glass cover slips (24 mm × 24 mm, 0.13–0.17 mm thick, Fisherbrand™, Fisher
248 Scientific AG, Switzerland) are placed under the PFA tubing to further improve contrast. To ensure that
249 temperature measurements are representative of actual droplet temperatures, two thermocouples (K-type, 0.5 mm
250 OD, RS Components GmbH, Germany, and TC Direct, Germany) are placed horizontally in the ethanol bath in
251 the same plane as the PFA tubing (Fig. 1b), with the average of the recorded temperatures taken to be
252 representative of the temperature of the droplets. Each thermocouple was calibrated to the melting point of
253 mercury (−38.8 °C or 234.4 K) and water (0 °C or 273.15 K), providing a high accuracy with a standard deviation
254 of 0.1 K for three measurements at each melting point. Over all experiments reported herein, the average difference
255 in the measured temperature between the two thermocouples ($T_2 - T_1$) in the ethanol bath was 0.01 ± 0.21 K
256 (standard deviation). The uncertainty in our temperature measurement is thus reported to be ± 0.2 K.

257

258 A Peltier element (PKE 128A 0020 HR 150, Peltron GmbH, Germany) is connected to a laptop-controlled power
259 supply (Manson® HCS-3302, Distrelec Group AG, Switzerland) to achieve the user-defined cooling rate. Heat
260 from the Peltier element is dissipated from below by an aqueous 55 % v/v ethylene glycol (98 % technical grade,
261 Sigma–Aldrich, USA) mixture circulating through an aluminium block connected to a chiller (Huber KISS K6,
262 Huber Kältemaschinenbau AG, Germany). Thermal paste (Fischer Elektronik GmbH, Germany) is applied
263 between the top of the aluminium block and the bottom of the Peltier element to ensure good thermal contact.



264

265 A custom Python-based (Python 3.0) user interface was designed to permit the user to select the desired cooling
266 rate and image acquisition settings. Once these parameters are selected and the temperature of the ethanol bath
267 has reached steady state (with the chiller set to $-15\text{ }^{\circ}\text{C}$ and the power supply at 0.8 V), cooling is initiated. A
268 proportional controller with a temperature-dependent gain parameter sets the voltage of the power supply to
269 maintain this cooling rate (see Figs. B1 and B2 for the time series of cooling rate as a function of temperature for
270 each experiment reported herein). During cooling at 1 K min^{-1} , images are captured every three seconds, and the
271 temperature is recorded. Once the measured temperature reaches the set end temperature, e.g. 233 K, the program
272 terminates.

273 **2.4.3 Droplet size distribution**

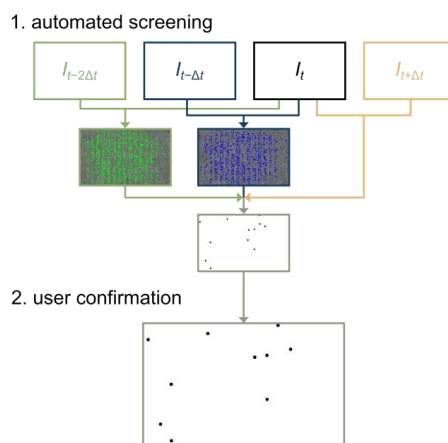
274 From a 10 second video of droplet generation, the mean droplet size is determined through a series of image
275 processing steps implemented in Python (using the cv2 and skimage packages): subtracting the background,
276 equalizing the histogram, morphological opening, thresholding, and using the Hough circle transform to identify
277 and measure the droplets in each frame of the captured video. The obtained mean diameter for each droplet
278 population is summarized in Table 1 and Table 2 for pure water and microcline suspensions, respectively. The
279 uncertainty in mean diameter is estimated to be $\pm 5\text{ }\mu\text{m}$ (corresponding to an uncertainty of 2 pixels in the droplet
280 radius).

281 **2.4.4 Freezing detection**

282 Due to the high purity of the SA water, only a weak increase in brightness is detected when a droplet freezes (i.e.,
283 the raw change in pixel intensity between the background and an unfrozen droplet vs. a frozen droplet is minimal),
284 possibly because few impurities are present to induce crystallographic defects that manifest as an increase in
285 brightness. Therefore, when combined with a low number of pixels per droplet, the detection of droplet freezing
286 in the saved images is challenging and necessitates a semi-automated approach.

287

288 An overview of the workflow for detecting droplet freezing is illustrated in Figure 3. If necessary, prior to
289 automated screening, an image stabilization routine is applied to the images using the cv2 and skimage packages
290 in Python for feature detection and Euclidian transformation. To detect droplet freezing, the images are first
291 automatically screened to find locations where droplet freezing may have occurred. Second, the user is prompted
292 to classify whether freezing did or did not occur. In the future, the manually-labelled images of frozen or unfrozen
293 droplets could be used to train a machine learning algorithm for fully-automated image processing. Droplets that
294 exhibit a clear spike in brightness upon freezing would facilitate the automation of image classification. A distinct
295 brightness change is expected for droplets containing solid impurities, such as INPs, or aqueous solutions of, for
296 example, NaCl.



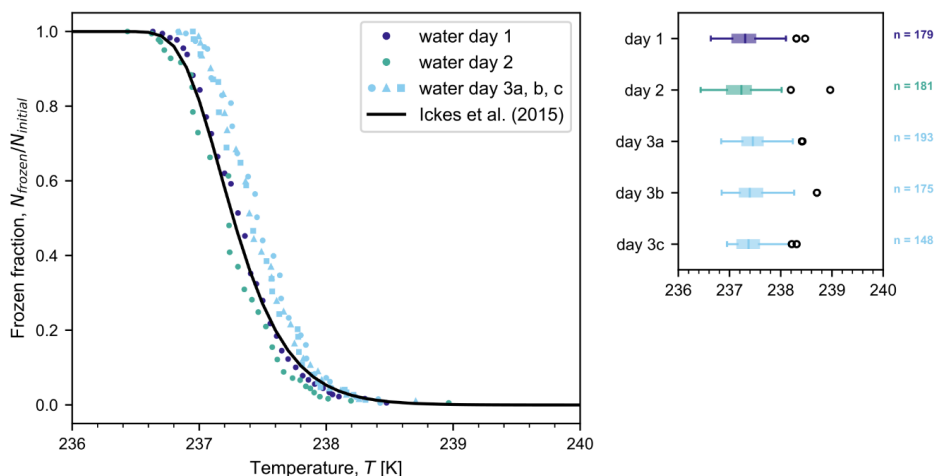
297
298 **Figure 3. Workflow to locate the droplets that froze between two consecutive images (I_t and $I_{t-\Delta t}$), also making use of**
299 **images $I_{t-2\Delta t}$ and $I_{t+\Delta t}$. The first step is to automatically screen potential locations where a droplet may have frozen,**
300 **by comparing the brightness change in a location between two consecutive images I_t and $I_{t-\Delta t}$ (potential freezing**
301 **events highlighted with blue pixels). During this first step, we also screen for false positives due to droplet motion or**
302 **impurities in the ethanol bath by analyzing additional images $I_{t-2\Delta t}$ (potential freezing events highlighted with green**
303 **pixels) and $I_{t+\Delta t}$ for brightness changes at the same pixel coordinate. The second step is for the user to confirm whether**
304 **a droplet actually froze at that location (to eliminate false positives due to noise or other optical interference).**

305
306 The automated screening procedure includes multiple steps: subtracting the pixel intensities of two consecutive
307 images taken at time t and $t - \Delta t$, applying a bilateral filter to the subtracted image, carrying out morphological
308 opening, detecting edges, and applying a Hough circle transform to find potential droplet centres. To reduce the
309 number of potential droplets that must be classified by the user, the above procedure is always performed for two
310 pairs of images, resulting in the difference images $I_{-\Delta t} = I_t - I_{t-\Delta t}$ (with potential droplet centres highlighted
311 in blue in Figure 3) and $I_{-2\Delta t} = I_t - I_{t-2\Delta t}$ (with potential droplet centres highlighted in green in Figure 3).
312 Only those coordinates where brightness changes are detected in both image pairs are considered as potential
313 freezing events. Additionally, two criteria were defined that must be met in the $I_{-\Delta t}$ image to definitively tag a
314 droplet: (i) the identified coordinate must fall within a predefined grid of pixels where tubing is present; (ii) the
315 average pixel intensity of an 8-pixel radius at that coordinate must be less than 90 (i.e., dark in the range of
316 grayscale values between 0 and 255). Finally, the average pixel intensity of an 8-pixel radius at that coordinate in
317 the $I_{+\Delta t} = I_{t+\Delta t} - I_t$ image must be less than 150. The user can also flag any frozen droplets that are not
318 spherical as a result of two droplets coalescing. These frozen droplets with twice the volume are discarded from
319 further analysis.
320



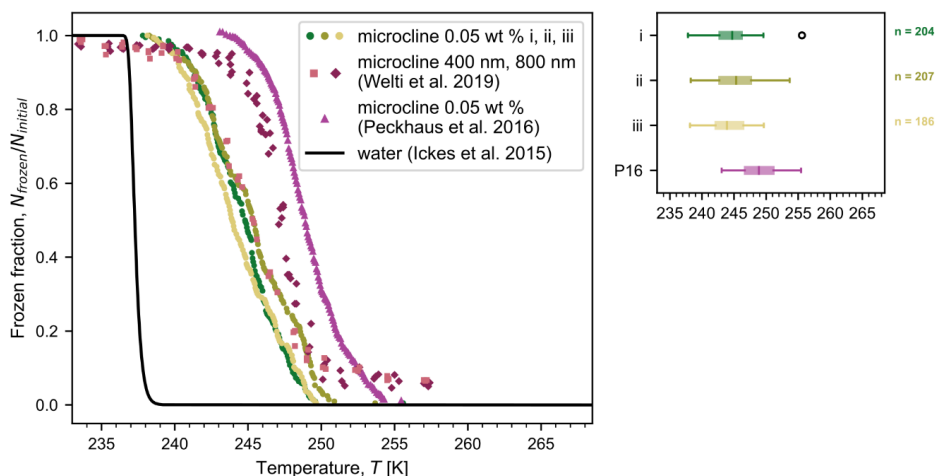
321 **3 Results and Discussion**

322 Figure 4 depicts the fraction of frozen droplets as a function of temperature for three independent droplet
323 populations of Sigma–Aldrich (SA) water cooled at a rate of 1 K min^{-1} . After being frozen once, the third droplet
324 population was thawed and refrozen twice more (day 3b and 3c). In each frozen fraction curve, there is a single
325 data point corresponding to each saved image (that is, one data point at every interval of 0.05 K showing the
326 cumulative number of droplets frozen down to that temperature). From the three independent droplet populations,
327 the median freezing temperature is reproducible within a narrow temperature range of $237.3 \pm 0.1 \text{ K}$ (standard
328 deviation). Possible contributions to the observed variability could arise from inherent uncertainty in the
329 thermocouple measurement, small changes in the positioning of the tubing holder and thermocouples between
330 experiments, and/or slight differences in droplet diameter between droplet populations. The repeated freeze–thaw
331 cycles yield an even narrower median temperature range of $237.41 \pm 0.04 \text{ K}$ (standard deviation), a variability
332 that can be attributed solely to inherent uncertainty in the thermocouple measurement, because there were no
333 changes to the droplet population or to the positioning of the holder or thermocouples. Given the high
334 reproducibility of results over three freezing cycles, MINCZ is ideally suited for investigating questions
335 surrounding the stochasticity of nucleation in a single droplet, in contrast to continuous flow microfluidic devices
336 that are well-suited for high-throughput analysis when detecting the presence of rare ice-nucleating particles. For
337 comparison, Figure 4 also shows the frozen fraction calculated based on the recommended parameterization for
338 the homogeneous nucleation rate of water from Ickes et al. (2015) (see Appendix C for more details), which was
339 obtained by fitting to a wide range of previously-reported experimental data and is representative of current state-
340 of-the-art. The frozen fractions observed using MINCZ are in general agreement with this parameterization. The
341 accurate and reproducible results for the median freezing temperature of pure water droplets and the lack of an
342 early freezing onset validates MINCZ as a reliable instrument that can be used to detect freezing due to mediocre
343 ice-nucleating particles at any temperature above the onset of homogeneous ice nucleation. Early freezing onset
344 can occur due to impurities present in the pure water sample that would appear, for example, as a slow increase
345 in frozen fraction at higher temperatures, as seen in the freezing behaviour of pure water in Peckhaus et al. (2016)
346 and Brubaker et al. (2019). The ability of MINCZ to reach such low temperatures is achieved with very low
347 droplet volumes (approx. 200 pL) and the absence of a solid substrate that may initiate the nucleation of ice at
348 higher temperatures. Lastly, we confirmed that there is no spatial bias in freezing behaviour across the observed
349 area, as summarized in Appendix B.



350
351 **Figure 4.** Frozen fraction of pure water (Sigma–Aldrich) droplets (with diameters as indicated in Table 1) as a
352 function of temperature for different droplet populations (with n number of droplets) cooled at a rate of 1 K min^{-1} on
353 three separate days. The droplet population on day 3 was subjected to three freeze–thaw cycles (a, b, c). Also shown is
354 the frozen fraction curve for the homogeneous freezing of water using the parameterization from Ickes et al. (2015)
355 for droplets with a diameter of $75 \mu\text{m}$. Boxplots on the right-hand side summarize the experimental results. The
356 center line of each boxplot indicates the median freezing temperature, the box spans the interquartile range (between
357 the 25th and 75th percentiles), the whiskers extend to the maximum and minimum temperatures, and outliers are
358 shown by open circles. The temperature uncertainty of our measurements is estimated to be $\pm 0.2 \text{ K}$.

359 Figure 5 shows the frozen fraction of droplets as a function of temperature for aqueous suspensions containing
360 0.05 wt % microcline, also cooled at a rate of 1 K min^{-1} . Three independent droplet populations were generated
361 and cooled, yielding a median freezing temperature of $244.6 \pm 0.7 \text{ K}$. As in Figure 4, one data point is plotted for
362 every 0.05 K interval in temperature, showing the cumulative number of droplets frozen down to that temperature.
363 In comparison to the results for pure water, droplets containing microcline particles froze at higher temperatures
364 and over a wider range. Additionally, the standard deviation of the median freezing temperature increased,
365 showing a higher variability between runs. This widening of freezing temperature and increase in variability
366 relative to that seen for homogeneous freezing can be explained by inherent variations in the amount and activity
367 of the mineral particles present in each droplet. As investigated by Knopf et al. (2020), variations in the surface
368 area of the mineral in each droplet can be one source of variability in the frozen fraction. In Figure 5, we also
369 show results reported by Welti et al. (2019) using the same microcline sample, but studied using the Zurich Ice
370 Nucleation Chamber (ZINC) with particles size-selected to a mobility diameter of 400 nm or 800 nm. Finally, in
371 Figure 5, we also include the frozen fraction of water droplets (~ 750 droplets with volumes of 0.2 nL) containing
372 0.05 wt % microcline (sample named FS02) printed onto a solid substrate and cooled at 1 K min^{-1} by Peckhaus
373 et al. (2016). Both mineral samples were predominantly microcline ($\sim 90 \%$ K-feldspar and $\sim 10 \%$ Na-feldspar in
374 Welti et al. (2019); 80 % K-feldspar, 16 % Na/Ca-feldspar, and 4 % quartz in Peckhaus et al. (2016)). Overall, the
375 frozen fraction curves obtained from MINCZ and ZINC show ice nucleation activity of the microcline particles
376 in a similar temperature regime, with freezing in MINCZ occurring at temperatures close to those of the 400 nm
377 particles in ZINC; all of these frozen fraction curves are at lower temperatures compared to the data obtained by
378 Peckhaus et al. (2016).



379

380 **Figure 5.** Frozen fraction of microcline (0.05 wt % in SA water) droplets (with diameters as indicated in Table 2) as a
381 function of temperature for three independent droplet populations (i, ii, iii with n number of droplets) cooled at a rate of
382 1 K min^{-1} . For comparison, we show experimental results reported in Welti et al. (2019) obtained with the same
383 microcline sample but using the Zurich Ice Nucleation Chamber (ZINC) for particles size-selected to a mobility
384 diameter of 400 nm or 800 nm. The frozen fraction curve digitized from Peckhaus et al. (2016) (P16 in the boxplot) is
385 also shown for comparison, where 0.2 nL aqueous droplets with 0.05 wt % microcline suspension were printed onto a
386 solid substrate and cooled at 1 K min^{-1} . Also illustrated is the frozen fraction curve for the homogeneous freezing of
387 water using the parameterization from Ickes et al. (2015) for droplets with a diameter of $75 \mu\text{m}$. On the right, a
388 boxplot compares the freezing temperatures of the three droplet populations, where the center line indicates the
389 median freezing temperature, the box spans the interquartile range (between the 25th and 75th percentiles), the
390 whiskers extend to the maximum and minimum temperatures, and outliers are shown by open circles. The
391 temperature uncertainty of our measurements is estimated to be $\pm 0.2 \text{ K}$.

392 We note that the curves obtained using MINCZ depend on the concentration of microcline in suspension, since
393 any change to the available surface area will shift the observed temperature of ice nucleation accordingly. For our
394 concentration of 0.05 wt%, the expected surface area is on the order of 10^{-10} m^2 (assuming a Brunauer–Emmett–
395 Teller (BET) adsorption specific surface area between $1.9 \text{ m}^2 \text{ g}^{-1}$ (Atkinson et al., 2013) and $3.2 \text{ m}^2 \text{ g}^{-1}$ (Kumar et
396 al., 2018)). In contrast, single particles were investigated using ZINC with surface areas on the order of 10^{-13} to
397 10^{-12} m^2 for 400 nm and 800 nm, respectively. Typically, median freezing temperatures increase as particle surface
398 areas increase (e.g., as seen in Welti et al. (2019)), because there is an increased probability that the surface
399 contains a nucleation site that is active at higher temperatures. Since the surface area of microcline per droplet in
400 MINCZ is at least two orders of magnitude larger than that of a single particle, it may be expected that the median
401 freezing temperature of these droplets would be at a higher temperature than the median freezing temperature of
402 droplets with a single particle in ZINC. However, we observe that the frozen fraction curves obtained with MINCZ
403 are in agreement with the 400 nm particles analysed in ZINC, but freeze at lower temperatures compared to the
404 800 nm particles analysed in ZINC. This could be explained by a mineralogical bias due to 450 nm filtration of
405 the solution used in MINCZ that shifts freezing towards lower temperatures. That is, the larger particles may
406 exhibit a higher density of active sites that induce freezing at higher temperatures because of a size-dependent
407 mineralogical composition or morphology, and as a result, increasing the surface area by increasing only the
408 number of sub-450 nm particles in the droplets would not increase the probability of nucleation. Alternatively, if



409 there was in fact no mineralogical bias depending on particle size, the activity of the microcline could have instead
410 decreased over its storage time as a dry sample over a period of seven years from when it was previously analysed
411 in ZINC.

412

413 Finally, we can compare the frozen fraction of microcline suspensions studied using MINCZ to that obtained by
414 Peckhaus et al. (2016), where the same microcline concentration was investigated (0.05 wt%) at the same cooling
415 rate of 1 K min^{-1} . The main difference between these two studies was in sample preparation: we sonicated and
416 filtered the microcline suspension prior to cooling, but the sample was only suspended in solution after milling
417 the stone sample in Peckhaus et al. (2016). Similar to the discrepancy in the frozen fractions between MINCZ and
418 ZINC, it is again not possible to determine why the observed frozen fraction is at lower temperatures compared
419 to the data in Peckhaus et al. (2016). Either there could have been a mineralogical bias due to 450 nm filtration,
420 or the activity of the microcline sample studied herein could have been lower than the activity of the sample
421 studied by Peckhaus et al. (2016). An inherent difference in ice nucleation activity of two microcline samples
422 collected at different locations has also been observed by Kaufmann et al. (2016), who investigated the same
423 sample from Elba as Welti et al. (2019) and a sample from Namibia. They found that the sample from Namibia
424 exhibited a higher ice nucleation activity than the one from Elba despite its lower microcline content.

425 **4 Conclusions**

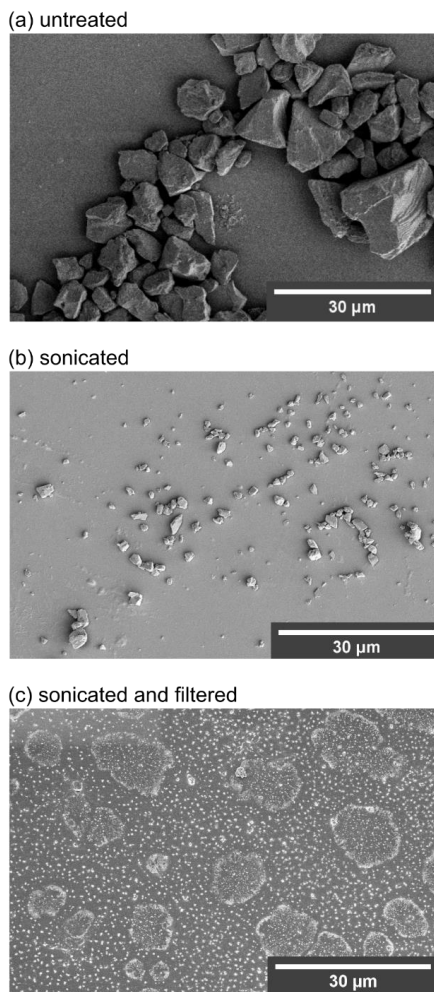
426 The MINCZ platform employs microfluidic technology to generate homogeneously-sized droplet populations of
427 approximately $75 \mu\text{m}$ in diameter that are then cooled off-chip in PFA tubing immersed in ethanol. We presented
428 the validation of this technique for the homogeneous freezing of pure water as well as heterogeneous freezing
429 using microcline. Our obtained results in the temperature range of homogeneous freezing fit well within the
430 expected temperature ranges reported previously. By immersing the tubing containing the droplets in a cooling
431 bath, MINCZ cools the droplets from all directions, instead of only from below, reducing the temperature gradient
432 and therefore yielding a high temperature accuracy of 0.2 K. The lack of early-onset freezing events in our data
433 obtained for homogeneous nucleation indicates that there are very few, if any, impurities in the water used in this
434 work. Therefore, in future studies this characteristic allows the delineation between freezing due to the
435 homogeneous pathway and freezing due to mediocre or poor INPs that are only active at relatively low
436 temperatures. We showed that by storing droplets in gas-impermeable PFA tubing, multiple highly-reproducible
437 refreezing cycles can be performed. The semi-automated approach for freezing droplet detection allows for the
438 study of statistically high numbers of droplets (in excess of 10^2) in parallel. Furthermore, the instrument is
439 comprised of simple components (e.g., stereoscope, Peltier element, chiller, and CMOS camera), and it has a
440 relatively small footprint in the lab. These attributes make MINCZ also suitable for transfer to other laboratories
441 or field sites. Future work will focus on further automation of the operation of MINCZ to ensure continued
442 reproducibility by limiting user-dependent influences.

443



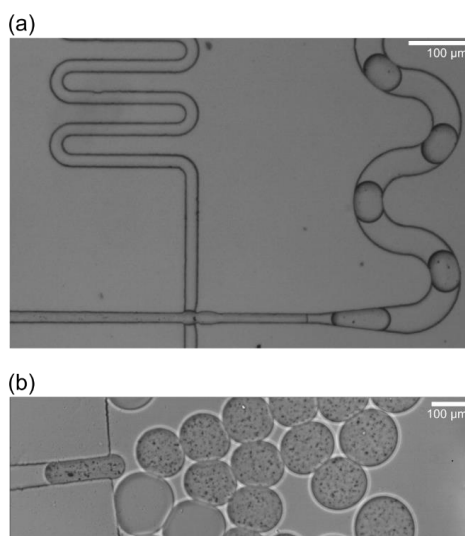
444 **Appendix A: Microcline particle imaging**

445 Figure A1 shows secondary electron (SE) scanning electron microscopy (SEM) images of microcline suspensions
446 that were (a) untreated, (b) sonicated with 8×30 s pulses in an ultrasonic VialTweeter, and (c) sonicated followed
447 by filtration ($0.45 \mu\text{m}$ polyethersulfone sterile syringe filter). Figure A2 shows images of microfluidic droplets
448 with untreated microcline suspensions at two concentrations ($0.1 \text{ wt } \%$ and $2 \text{ wt } \%$), where the heterogeneity in
449 microcline particle size is clearly visible. While sonication successfully broke apart the microcline particles, a
450 significant portion of larger particles remained (Fig. A1b). After sonication and filtration, the remaining particles
451 were more uniform in size (Fig. A1c).



452
453 **Figure A1.** Scanning electron microscopy images of microcline that was (a) untreated, (b) sonicated with 8×30 s pulses
454 in an ultrasonic VialTweeter, and (c) sonicated using the same procedure as (b) but additionally filtered ($0.45 \mu\text{m}$
455 syringe filter).

456
457



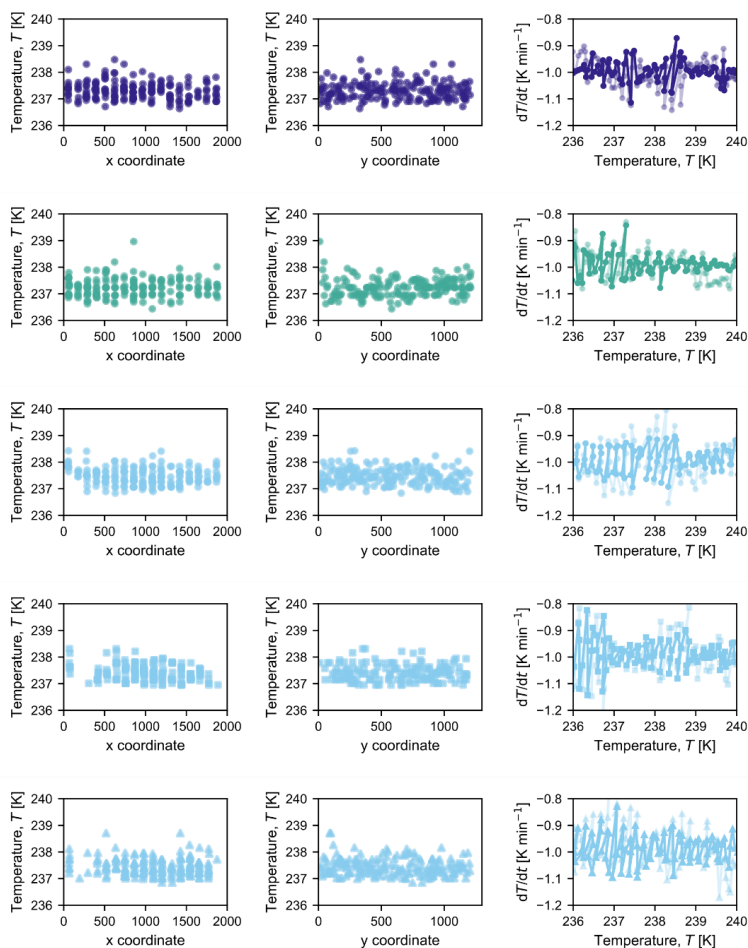
458
459 **Figure A2.** Microfluidic droplets of aqueous suspensions containing (a) 0.1 wt % and (b) 2 wt % microcline that were
460 neither sonicated nor filtered. Microcline particles in these droplets are clearly visible as black pixels in both images.
461 The slight difference in droplet sizes can be accounted to partial clogging of the droplet generating orifice due to the
462 high concentration of large mineral particles in this particular experimental run.



463 **Appendix B: Spatial distribution of freezing events and cooling rate for each experiment**

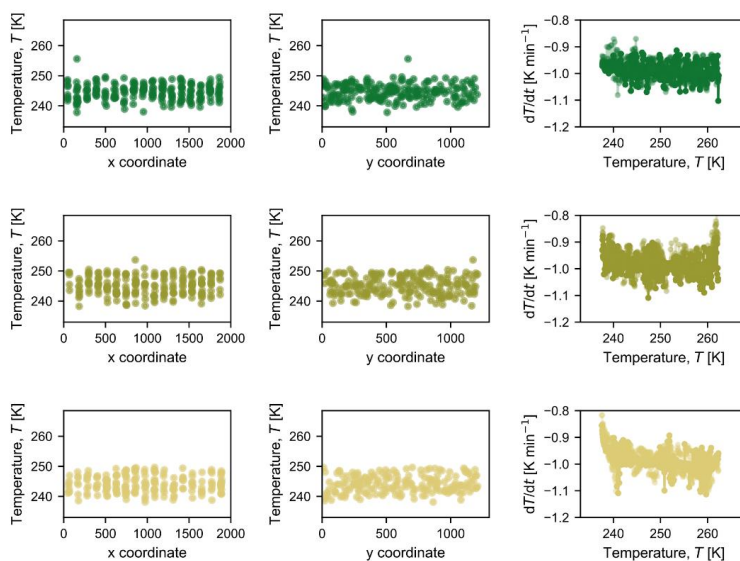
464 Figures B1 and B2 summarize the spatial temperature distribution of freezing events in the first two columns,
465 where each symbol represents one droplet freezing at a specific temperature and x - or y -coordinate. Over all
466 experiments (Fig. B1 for pure water and Fig. B2 for microcline suspensions), it is evident that there is no spatial
467 bias in freezing behaviour. The third column of each figure shows the measured cooling rate over the course of
468 each experiment, calculated based on the previous 60 s at each temperature where an image was saved (i.e.,
469 $dT/dt = (T(t) - T(t - 60 \text{ s})) / (60 \text{ s})$).

470



471

472 **Figure B1.** Compilation of observed freezing temperatures at each x - and y - pixel location to illustrate that there is no
473 discernable spatial bias in freezing temperature for each experiment conducted with pure water in Figure 4 (from top
474 to bottom: water day 1, water day 2, and water day 3a, b, and c). The third graph in each row shows the measured
475 cooling rate at each temperature where a picture was taken; the opaque line indicates the cooling rate measured by the
476 thermocouple that was used as input to the control loop, and the semi-opaque line indicates the cooling rate measured
477 by the second thermocouple in the bath.



478

479 **Figure B2. Compilation of observed freezing temperatures at each x - and y - pixel location to illustrate that there is no**
480 **discernable spatial bias in freezing temperature for each experiment conducted with the microcline suspension shown**
481 **in Figure 5 (from top to bottom: i, ii, and iii). The third graph in each row shows the measured cooling rate at each**
482 **temperature where a picture was taken; the opaque line indicates the cooling rate measured by the thermocouple that**
483 **was used as input to the control loop, and the semi-opaque line indicates the cooling rate measured by the second**
484 **thermocouple in the bath.**

485



486 **Appendix C: Calculation of frozen fraction from nucleation rate**

487

488 Following the derivation in Pruppacher and Klett (2010, p.211), the differential number of droplets that remains
489 unfrozen in a differential time can be integrated to yield

$$f_{\text{un}} = \frac{N_{\text{un}}}{N_0} = \exp(-V_d J_{\text{hom}} t) \quad (\text{C1})$$

490 where f_{un} is the fraction of droplets that remains unfrozen (where N_{un} is the number of unfrozen droplets after
491 time t , and N_0 is the total number of unfrozen droplets at time $t = 0$), V_d is the volume of a droplet, and J_{hom} is
492 the homogeneous nucleation rate.

493

494 To evaluate our experiments, we count the frozen droplets at fixed time intervals, Δt . As we cool the droplets at
495 a rate of 1 K min^{-1} , we evaluate Eq. (C1) every 6 s to obtain a temperature resolution of 0.1 K. We account for
496 the depletion of droplets using the following equation:

$$f_{i,\text{un}} = \frac{N_{i,\text{un}}}{N_0} = \exp(-V_d J_{\text{hom}} \Delta t) f_{i-1,\text{un}} \quad (\text{C2})$$

497 where $f_{i,\text{un}}$ is the fraction of droplets that remained unfrozen at T_i , $f_{i-1,\text{un}}$ is the unfrozen fraction of droplets at
498 T_{i-1} , and $\Delta t = 6 \text{ s}$.

499

500 For comparison with our experiments, we use the homogeneous nucleation rate parameterization by Ickes et al.
501 (2015):

$$J_{\text{hom}} = C \exp\left(-\frac{\Delta g^\#}{k_B T}\right) \exp\left(-\frac{\Delta G}{k_B T}\right) \quad (\text{C3})$$

502

503 where $C = 10^{35} \text{ cm}^{-3} \text{ s}^{-1}$, k_B is the Boltzmann constant, T is temperature, and $\Delta g^\#$ and ΔG are the diffusional
504 activation energy and thermodynamic energy barrier, respectively, calculated as follows (Zobrist et al., 2007):

$$\Delta g^\# = \frac{892 \text{ K } k_B T^2}{(T - 118 \text{ K})^2} \quad (\text{C4})$$

$$\Delta G = \frac{16\pi}{3} \frac{v_{\text{ice}}^2(T) \sigma_{\text{sl}}^3(T)}{(k_B T \ln S(T))^2} \quad (\text{C5})$$

505

506 where the molecular volume of ice v_{ice} and the saturation ratio S (ratio between the equilibrium vapour pressure
507 of supercooled liquid and that of ice) depend on temperature using the parameterizations outlined in Zobrist et al.
508 (2007), while the solid–liquid interfacial tension σ_{sl} is calculated using the parameterization from Reinhardt and
509 Doye (2013):

$$\sigma_{\text{sl}} [\text{N} \cdot \text{cm}^{-1}] = 3 \times 10^{-6} - 1.8 \times 10^{-8} (273.15 - T) \quad (\text{C6})$$

510



511 *Code and data availability.* Plot data are compiled in the ETH Research Collection data repository at
512 doi:10.3929/ethz-b-000545467. Python scripts are available upon request. *Note from authors: The link will be*
513 *activated after acceptance of the manuscript for final publication.*

514

515 *Author contributions.* FNI and NS are co-first authors of the manuscript and contributed equally to the instrument
516 design, generation of data, data analysis, and writing of the original draft; as such, they may each list their name
517 first in their CV. All authors contributed to project conceptualization, methodology, writing (review and editing),
518 and have approved the final version of the manuscript.

519

520 *Competing interests.* At least one of the (co-)authors is a member of the editorial board of Atmospheric
521 Measurement Techniques. The peer-review process was guided by an independent editor, and the authors have
522 also no other competing interests to declare.

523

524 *Acknowledgements.* We acknowledge work by Roland Walker who machined and 3D-printed portions of the
525 instrument, Fredy Mettler who provided support for the Peltier element, and Benedikt Waser who calculated the
526 calibration equations for the thermocouples. We also appreciate technical advice from Cyril Brunner and Kunfeng
527 Gao, as well as helpful discussions with Naama Reicher, Ulrich Krieger and Thomas Peter.

528

529 *Financial support.* NS acknowledges support from an ETH Postdoctoral Fellowship (20-1 FEL-46) and a Natural
530 Sciences and Engineering Research Council of Canada (NSERC) Postdoctoral Fellowship.

531



532 **References**

- 533 Assegehegn, G., Brito-de la Fuente, E., Franco, J. M. and Gallegos, C.: The importance of understanding the
534 freezing step and its impact on freeze-drying process performance, *J. Pharm. Sci.*, 108(4), 1378–1395,
535 doi:10.1016/j.xphs.2018.11.039, 2019.
- 536 Atig, D., Touil, A., Ildefonso, M., Marlin, L., Bouriat, P. and Broseta, D.: A droplet-based millifluidic method
537 for studying ice and gas hydrate nucleation, *Chem. Eng. Sci.*, 192, 1189–1197, doi:10.1016/j.ces.2018.08.003,
538 2018.
- 539 Atkinson, J. D., Murray, B. J., Woodhouse, M. T., Whale, T. F., Baustian, K. J., Carslaw, K. S., Dobbie, S.,
540 O’Sullivan, D. and Malkin, T. L.: The importance of feldspar for ice nucleation by mineral dust in mixed-phase
541 clouds, *Nature*, 498(7454), 355–358, doi:10.1038/nature12278, 2013.
- 542 Brubaker, T., Polen, M., Cheng, P., Ekambaram, V., Somers, J., Anna, S. L. and Sullivan, R. C.: Development
543 and characterization of a “store and create” microfluidic device to determine the heterogeneous freezing
544 properties of ice nucleating particles, *Aerosol Sci. Technol.*, 54(1), 79–93,
545 doi:10.1080/02786826.2019.1679349, 2019.
- 546 David, R. O., Cascajo-Castresana, M., Brennan, K. P., Rösch, M., Els, N., Werz, J., Weichlinger, V., Boynton,
547 L. S., Bogler, S., Borduas-Dedekind, N., Marcolli, C. and Kanji, Z. A.: Development of the DRoplet Ice Nuclei
548 Counter Zurich (DRINCZ): validation and application to field-collected snow samples, *Atmos. Meas. Tech.*, 12,
549 6865–6888, doi:10.3929/ethz-a-010782581, 2019.
- 550 Deck, L. T., Ochsenein, D. R. and Mazzotti, M.: Stochastic shelf-scale modeling framework for the freezing
551 stage in freeze-drying processes, *Int. J. Pharm.*, 613, 121276, doi:10.1016/j.ijpharm.2021.121276, 2022.
- 552 Diehl, K., Debertshäuser, M., Eppers, O., Schmithüsen, H., Mitra, S. K. and Borrmann, S.: Particle surface area
553 dependence of mineral dust in immersion freezing mode: Investigations with freely suspended drops in an
554 acoustic levitator and a vertical wind tunnel, *Atmos. Chem. Phys.*, 14(22), 12343–12355, doi:10.5194/acp-14-
555 12343-2014, 2014.
- 556 Edd, J. F., Humphry, K. J., Irimia, D., Weitz, D. A. and Toner, M.: Nucleation and solidification in static arrays
557 of monodisperse drops, *Lab Chip*, 9(13), 1859–1865, doi:10.1039/b821785h, 2009.
- 558 Garcia, E., Hill, T. C. J., Prenni, A. J., DeMott, P. J., Franc, G. D. and Kreidenweis, S. M.: Biogenic ice nuclei
559 in boundary layer air over two U.S. high plains agricultural regions, *J. Geophys. Res. Atmos.*, 117(17), 1–12,
560 doi:10.1029/2012JD018343, 2012.
- 561 Harrison, A. D., Whale, T. F., Carpenter, M. A., Holden, M. A., Neve, L., O’Sullivan, D., Vergara Temprado, J.,
562 Murray, B. J.: Not all feldspars are equal: A survey of ice nucleating properties across the feldspar group of
563 minerals, *Atmos. Chem. Phys.*, 16(17), 10927–10940, doi:10.5194/acp-16-10927-2016, 2016.
- 564 Heyries, K. A., Tropini, C., Vaninsberghe, M., Doolin, C., Petriv, O. I., Singhal, A., Leung, K., Hughesman, C.
565 B. and Hansen, C. L.: Megapixel digital PCR, *Nat. Methods*, 8(8), 649–651, doi:10.1038/nmeth.1640, 2011.
- 566 Ickes, L., Welti, A., Hoose, C. and Lohmann, U.: Classical nucleation theory of homogeneous freezing of water:



- 567 Thermodynamic and kinetic parameters, *Phys. Chem. Chem. Phys.*, 17(8), 5514–5537,
568 doi:10.1039/c4cp04184d, 2015.
- 569 Kanji, Z. A., Ladino, L. A., Wex, H., Boose, Y., Burkert-Kohn, M., Cziczo, D. J. and Krämer, M.: Overview of
570 ice nucleating particles, *Meteorol. Monogr.*, 58, 1.1-1.33, doi:10.1175/AMSMONOGRAPHIS-D-16-0006.1,
571 2017.
- 572 Kaufmann, L., Marcolli, C., Hofer, J., Pinti, V., Hoyle, C. R. and Peter, T.: Ice nucleation efficiency of natural
573 dust samples in the immersion mode, *Atmos. Chem. Phys.*, 16(17), 11177–11206, doi:10.5194/acp-16-11177-
574 2016, 2016.
- 575 Kaufmann, L., Marcolli, C., Luo, B. and Peter, T.: Refreeze experiments with water droplets containing
576 different types of ice nuclei interpreted by classical nucleation theory, *Atmos. Chem. Phys.*, 17(5), 3525–3552,
577 doi:10.5194/acp-17-3525-2017, 2017.
- 578 Klumpp, K., Marcolli, C. and Peter, T.: The impact of (bio-)organic substances on the ice nucleation activity of
579 the K-feldspar microcline in aqueous solutions, *Atmos. Chem. Phys.*, 22(5), 3655–3673, doi:10.5194/acp-22-
580 3655-2022, 2022.
- 581 Knopf, D. A., Alpert, P. A., Zipori, A., Reicher, N. and Rudich, Y.: Stochastic nucleation processes and
582 substrate abundance explain time-dependent freezing in supercooled droplets, *npj Clim. Atmos. Sci.*, 3(1), 1–9,
583 doi:10.1038/s41612-020-0106-4, 2020.
- 584 Koop, T., Luo, B., Tsias, A. and Peter, T.: Water activity as the determinant for homogeneous ice nucleation in
585 aqueous solutions, *Nature*, 406, 611–614, 2000.
- 586 Krämer, B., Schwell, M., Hübner, O., Vortisch, H., Leisner, T., Rühl, E., Baumgärtel, H. and Wöste, L.:
587 Homogeneous ice nucleation observed in single levitated micro droplets, *Berichte der*
588 *Bunsengesellschaft/Physical Chem. Chem. Phys.*, 100(11), 1911–1914, doi:10.1002/bbpc.19961001120, 1996.
- 589 Kreidenweis, S. M., Petters, M. and Lohmann, U.: 100 Years of Progress in Cloud Physics, Aerosols, and
590 Aerosol Chemistry Research, *Meteorol. Monogr.*, 59, 11.1-11.72, doi:10.1175/AMSMONOGRAPHIS-D-18-
591 0024.1, 2018.
- 592 Kumar, A., Marcolli, C., Luo, B. and Peter, T.: Ice nucleation activity of silicates and aluminosilicates in pure
593 water and aqueous solutions - Part 1: The K-feldspar microcline, *Atmos. Chem. Phys.*, 18(10), 7057–7079,
594 doi:10.5194/acp-18-7057-2018, 2018.
- 595 Kunert, A. T., Lamneck, M., Helleis, F., Pöschl, U., Pöhlker, M. L. and Fröhlich-Nowoisky, J.: Twin-plate Ice
596 Nucleation Assay (TINA) with infrared detection for high-Throughput droplet freezing experiments with
597 biological ice nuclei in laboratory and field samples, *Atmos. Meas. Tech.*, 11(11), 6327, doi:10.5194/amt-11-
598 6327-2018, 2018.
- 599 Lohmann, U.: Anthropogenic aerosol influences on mixed-phase clouds, *Curr. Clim. Chang. Reports*, 3(1), 32–
600 44, doi:10.1007/s40641-017-0059-9, 2017.
- 601 Lohmann, U. and Feichter, J.: Global indirect aerosol effects: a review, *Atmos. Chem. Phys.*, 5, 715–737,



- 602 doi:10.5194/acpd-4-7561-2004, 2005.
- 603 Marquez-Curtis, L. A., Bokenfohr, R., McGann, L. E. and Elliott, J. A. W.: Cryopreservation of human cerebral
604 microvascular endothelial cells and astrocytes in suspension and monolayers, *PLoS One*, 16,
605 doi:10.1371/journal.pone.0249814, 2021.
- 606 Matus, A. V. and L'Ecuyer, T. S.: The role of cloud phase in Earth's radiation budget, *J. Geophys. Res.*, 122(5),
607 2559–2578, doi:10.1002/2016JD025951, 2017.
- 608 Metcalf, A. R., Narayan, S. and Dutcher, C. S.: A review of microfluidic concepts and applications for
609 atmospheric aerosol science, *Aerosol Sci. Technol.*, 52(3), 310–329, doi:10.1080/02786826.2017.1408952,
610 2018.
- 611 Miller, A. J., Brennan, K. P., Mignani, C., Wieder, J., David, R. O. and Borduas-Dedekind, N.: Development of
612 the drop Freezing Ice Nuclei Counter (FINC), intercomparison of droplet freezing techniques, and use of soluble
613 lignin as an atmospheric ice nucleation standard, *Atmos. Meas. Tech.*, 14(4), 3131–3151, doi:10.5194/amt-14-
614 3131-2021, 2021.
- 615 Murray, B. J., Carslaw, K. S. and Field, P. R.: Opinion: Cloud-phase climate feedback and the importance of
616 ice-nucleating particles, *Atmos. Chem. Phys.*, 21(2), 665–679, doi:10.5194/acp-21-665-2021, 2021.
- 617 Peckhaus, A., Kiselev, A., Hiron, T., Ebert, M. and Leisner, T.: A comparative study of K-rich and Na/Ca-rich
618 feldspar ice-nucleating particles in a nanoliter droplet freezing assay, *Atmos. Chem. Phys.*, 16(18), 11477–
619 11496, doi:10.5194/acp-16-11477-2016, 2016.
- 620 Pegg, D. E.: Principles of cryopreservation, in *Cryopreservation and Freeze-Drying Protocols*, pp. 3–19,
621 Springer, New York, NY., 2015.
- 622 Polen, M., Brubaker, T., Somers, J. and Sullivan, R. C.: Cleaning up our water: Reducing interferences from
623 nonhomogeneous freezing of “pure” water in droplet freezing assays of ice-nucleating particles, *Atmos. Meas.*
624 *Tech.*, 11(9), 5315–5334, doi:10.5194/amt-11-5315-2018, 2018.
- 625 Pruppacher, H. R. and Klett, J. D.: *Microphysics of Clouds and Precipitation*, Springer, Dordrecht., 2010.
- 626 Reicher, N., Segev, L. and Rudich, Y.: The Weizmann Supercooled Droplets Observation on a Microarray
627 (WISDOM) and application for ambient dust, *Atmos. Meas. Tech.*, 11(1), 233–248, doi:10.5194/amt-11-233-
628 2018, 2018.
- 629 Reinhardt, A. and Doye, J. P. K.: Note: Homogeneous TIP4P/2005 ice nucleation at low supercooling, *J. Chem.*
630 *Phys.*, 139(9), 096102, doi:10.1063/1.4819898, 2013.
- 631 Riechers, B., Wittbracht, F., Hütten, A. and Koop, T.: The homogeneous ice nucleation rate of water droplets
632 produced in a microfluidic device and the role of temperature uncertainty, *Phys. Chem. Chem. Phys.*, 15(16),
633 5873–5887, doi:10.1039/c3cp42437e, 2013.
- 634 Rogers, D. C.: Development of a continuous flow thermal gradient diffusion chamber for ice nucleation studies,



- 635 Atmos. Res., 22, 149–181, 1988.
- 636 Roy, P., House, M. L. and Dutcher, C. S.: A microfluidic device for automated high throughput detection of ice
637 nucleation of Snomax®, *Micromachines*, 12(3), 1–18, doi:10.3390/mi12030296, 2021a.
- 638 Roy, P., Mael, L. E., Hill, T. C. J., Mehndiratta, L., Peiker, G., House, M. L., Demott, P. J., Grassian, V. H. and
639 Dutcher, C. S.: Ice nucleating activity and residual particle morphology of bulk seawater and sea surface
640 microlayer, *ACS Earth Sp. Chem.*, 5(8), 1916–1928, doi:10.1021/acsearthspacechem.1c00175, 2021b.
- 641 Schneider, J., Höhler, K., Heikkilä, P., Keskinen, J., Bertozzi, B., Bogert, P., Schorr, T., Silas Umo, N., Vogel,
642 F., Brasseur, Z., Wu, Y., Hakala, S., Duplissy, J., Moiseev, D., Kulmala, M., Adams, M. P., Murray, B. J.,
643 Korhonen, K., Hao, L., Thomson, E. S., Castarède, D., Leisner, T., Petäjä, T. and Möhler, O.: The seasonal
644 cycle of ice-nucleating particles linked to the abundance of biogenic aerosol in boreal forests, *Atmos. Chem.
645 Phys.*, 21(5), 3899–3918, doi:10.5194/acp-21-3899-2021, 2021.
- 646 Stan, C. A., Schneider, G. F., Shevkoplyas, S. S., Hashimoto, M., Ibanescu, M., Wiley, B. J. and Whitesides, G.
647 M.: A microfluidic apparatus for the study of ice nucleation in supercooled water drops, *Lab Chip*, 9(16), 2293–
648 2305, doi:10.1039/b906198c, 2009.
- 649 Stetzer, O., Baschek, B., Lüönd, F. and Lohmann, U.: The Zurich Ice Nucleation Chamber (ZINC) - A new
650 instrument to investigate atmospheric ice formation, *Aerosol Sci. Technol.*, 42(1), 64–74,
651 doi:10.1080/02786820701787944, 2008.
- 652 Tarn, M. D., Sikora, S. N. F., Porter, G. C. E., Wyld, B. V., Alayof, M., Reicher, N., Harrison, A. D., Rudich,
653 Y., Shim, J. U. and Murray, B. J.: On-chip analysis of atmospheric ice-nucleating particles in continuous flow,
654 *Lab Chip*, 20(16), 2889–2910, doi:10.1039/d0lc00251h, 2020.
- 655 Tarn, M. D., Sikora, S. N. F., Porter, G. C. E., Shim, J. and Murray, B. J.: Homogeneous freezing of water using
656 microfluidics, *Micromachines*, 12(2), 1–23, doi:10.3390/mi12020223, 2021.
- 657 Welti, A., Lohmann, U. and Kanji, Z. A.: Ice nucleation properties of K-feldspar polymorphs and plagioclase
658 feldspars, *Atmos. Chem. Phys.*, 19(16), 10901–10918, doi:10.5194/acp-19-10901-2019, 2019.
- 659 Wright, T. P. and Petters, M. D.: The role of time in heterogeneous freezing nucleation, *J. Geophys. Res.*
660 *Atmos.*, 118(9), 3731–3743, doi:10.1002/jgrd.50365, 2013.
- 661 Zobrist, B., Koop, T., Luo, B. P., Marcolli, C. and Peter, T.: Heterogeneous ice nucleation rate coefficient of
662 water droplets coated by a nonadecanol monolayer, *J. Phys. Chem. C*, 111(5), 2149–2155,
663 doi:10.1021/jp066080w, 2007.
- 664 Zobrist, B., Marcolli, C., Peter, T. and Koop, T.: Heterogeneous ice nucleation in aqueous solutions: The role of
665 water activity, *J. Phys. Chem. A*, 112(17), 3965–3975, doi:10.1021/jp7112208, 2008.
- 666